4 Graphene and Graphene-Based Nanocomposites

Robert J Young

School of Materials, University of Manchester, Manchester, M13 9PL, UK

4.1. Introduction

The study of graphene is one of the most exciting topics in materials science and condensed matter physics (Geim and Novoselov, 2007) and graphene has good prospects for applications in a number of different fields (Novoselov, 2011; Geim, 2011). There has been a rapid rise of interest in the study of the structure and properties of graphene following the first report in 2004 of the preparation and isolation of single graphene layers in Manchester (Novoselov et al, 2004). It had previously been thought that the isolation of single-layer graphene would not be possible since such 2D crystals would be unstable thermodynamically and/or might roll up into scrolls if prepared as single atomic layers (Young et al, 2012). A large number of studies since 2004 have shown that this is certainly not the case. There was excitement about graphene initially because of its electronic properties, with its charge carriers exhibiting very high intrinsic mobility, having zero effective mass and being able to travel distances of microns at room temperature without being scattered (Geim and Novoselov, 2007). Thus the majority of the original research upon graphene had concentrated upon electronic properties, aimed at applications such as using graphene in electronic devices (Avouris, 2010).

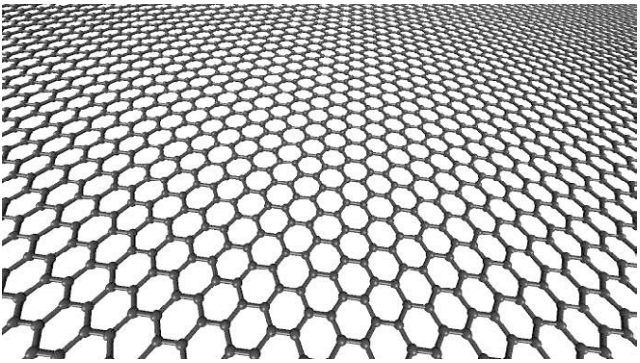

Figure 4.1. A molecular model of a single layer of graphene. (Courtesy of F. Ding, Hong Kong Polytechnic University). (Adapted from Young and Lovell, 2011 with permission from CRC Press).

O. Paris (Ed.), *Structure and Multiscale Mechanics of Carbon Nanomaterials*,
CISM International Centre for Mechanical Sciences
DOI 10.1007/ 978-3-7091-1887-0_4 © CISM Udine 2016

Graphene is the basic building block of all graphitic forms of carbon. It consists of a single atomic layer of sp^2 hybridized carbon atoms arranged in a honeycomb structure as shown in Figure 4.1. Research upon the material has now broadened considerably as it was soon realised that graphene might have other interesting and exciting physical properties such as high levels of stiffness and strength, and thermal conductivity, combined with an impermeability to gases. One obvious application of graphene is in the field of nanocomposites (Young et al, 2012) and researchers working upon other forms of nanocomposites, such as those reinforced by nanotubes or nanoclays, have now refocused their efforts towards graphene nanocomposites. Additionally there was pre-existing expertise in the exfoliation of graphite (e.g. expanded graphite) and in the preparation of graphene oxide (originally termed "graphite oxide"). The advantages and disadvantages of using graphene oxide in composite materials in comparison with pristine graphene has been discussed elsewhere (Young et al, 2012).

4.2. Graphene

4.2.1. Preparation

There has already been considerable effort put into the development of ways of preparing high-quality graphene in large quantities for both research purposes and with a view to possible applications (Rao et al, 2009). Since it was first isolated in 2004 several approaches have been employed to prepare the material. One is to break graphite down into graphene by techniques such as a mechanical cleavage or liquid phase exfoliation (sometimes termed "top-down"). The other methods is to synthesize graphene using techniques such as chemical vapour deposition (CVD) (often known as "bottom-up"), epitaxial growth on silicon carbide, molecular beam epitaxy, etc (Young et al, 2012).

Expanded graphite was developed more than 100 years as a filler for the polymer resins that were being developed at the same time and investigated extensively over the intervening period. More recently there have been developments in the preparation of thinner forms of graphite, known as graphite nanoplatelets (GNPs) (Kalaitzidou et al, 2007). They can be produced by a number of techniques that include the exposure of acid-intercalated graphite to microwave radiation, ball-milling and ultrasonication. The addition of GNPs to polymers has been found to lead to substantial improvements in mechanical and electrical properties at lower loadings than are needed with expanded graphite. The definition of GNPs covers all types of graphitic material from 100 nm thick platelets down to single layer graphene (Kalaitzidou et al, 2007). It is, however, the availability of single- or few-layer graphene that has caused the most excitement in recent times.

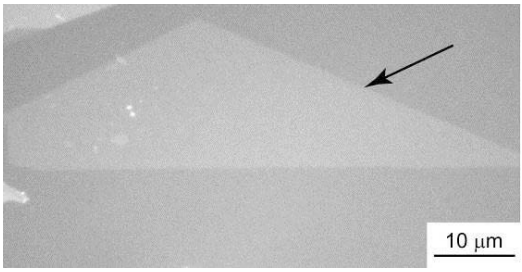

Figure 4.2. Optical micrograph of a graphene monolayer (indicated by an arrow) prepared by mechanical cleavage and deposited on a polymer substrate. (Adapted from Young and Lovell, 2011 with permission from CRC Press).

The simplest way of preparing small samples of single- or few-layer graphene is by the mechanical cleavage (i.e. the repeated peeling of graphene layers with adhesive tape) from either highly-oriented pyrolytic graphite or good-quality natural graphite (Novoselov et al, 2004). Figure 4.2 shows an optical micrograph of a sample of monolayer graphene prepared by mechanical cleavage and then deposited upon a polymer substrate. Typically, this method produces a mixture of one-, two- and many-layer graphene flakes that have dimensions of the order of tens of microns.

The rapid rise of interest in graphene for use in applications that require high volumes of material, such as in composites, led to investigations into methods of undertaking large-scale exfoliation. One of the first successful methods was the exfoliation and dispersion of graphite in organic solvents such as dimethylformamide or N-methylpyrrolidone (Hernandez et al, 2008). Depending on the levels of agitation and purification suspensions with large (>50%) fractions of graphene monolayers could be prepared. The material produced by this method is relatively free of defects and is not oxidised but the lateral dimensions of the graphene layers are typically no more than a few microns.

An important breakthrough has been the growth graphene films with macroscopic dimensions on the surfaces of metals. In the case of copper, growth takes place upon Cu foils via a surface-catalyzed process and thin metal films do not have to be employed (Suk et al, 2011). For both metals, it was found that the graphene films could be transferred to other substrates. This process has now been scaled-up to a roll-to-roll production process in which the graphene is grown by CVD on copper-coated rolls. It can then be transferred to a thin polymer film backed with an adhesive layer to produce transparent conducting films (Bae et al, 2010). It has been found that such films have a low electrical sheet resistance and optical transmittance of the order of 97.7%. They are found to be predominantly covered with a monolayer graphene film but also have some bilayer and multilayer islands.

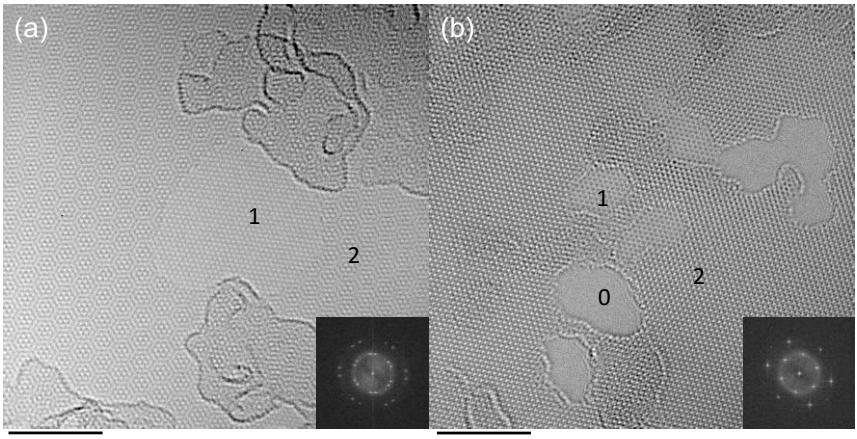

Figure 4.3. High resolution TEM image from CVD graphene showing regions of (a) non-Bernal stacking and (b) Bernal stacking (Scale bars = 5 nm). The selected area diffraction patterns are given and number of layers in the different areas is indicated (Courtesy of Jamie Warner and Sarah Haigh)

4.2.2. Characterisation

A single atomic layer of graphene absorbs ~2.3 % of visible light and its absorption is virtually independent of wavelength (Nair et al, 2008). Thus, being significantly optically active, graphene can be observed on certain substrates by simple methods, Figure 4.2. In fact, it is possible to distinguish between flakes of graphene with different numbers of layers relatively easily in a transmission optical microscope.

The atomic structure of graphene can be observed directly using transmission electron microscopy (TEM) (Meyer et al, 2007) as shown in Figure 4.3. It is relatively easy to resolve individual carbon atoms by TEM and the differences between Bernal-stacked and irregularly stacked material can be seen.

It is found that both an image of the graphene lattice and well-defined electron diffraction patterns can be obtained from suspended graphene sheets in the TEM (Meyer et al, 2007). The sheets, however, are not exactly flat but have static ripples out of plane on a scale of the order of 1 nm (Bangert et al, 2009). It was also found that there was no tendency for the graphene sheets to scroll or fold in contradiction to one of the preconceptions of its behaviour. Moreover, it was found that a sliver of graphene could extend nearly 10 μm from the edge of a metal TEM grid without any external support. This was taken as an indication that the graphene monolayers have a very high level of stiffness (Booth et al, 2008).

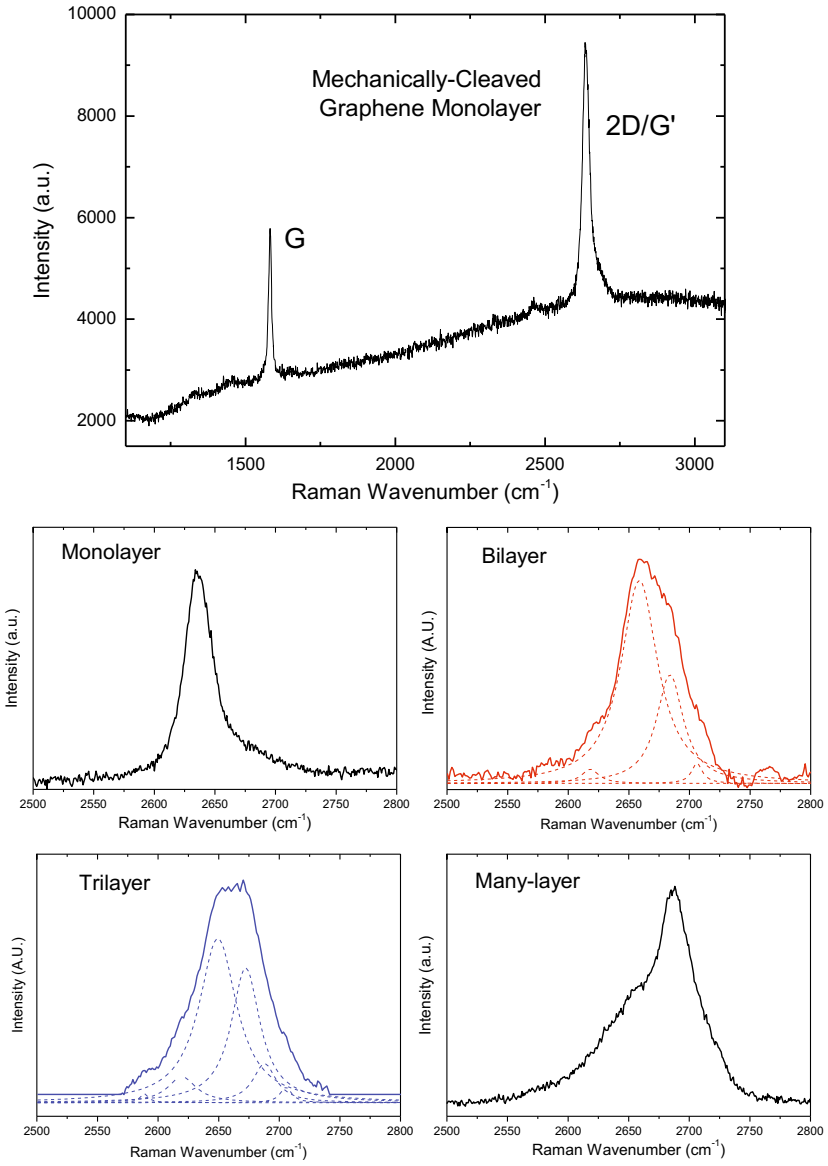

Figure 4.4. Raman spectra of monolayer graphene showing full spectrum with the G and 2D/G' bands (top). Details of the 2D/G' band for monolayer, bilayer, trilayer and many-layer materials (bottom).

Raman spectroscopy is a particularly useful technique to characterize graphene monolayers, bilayers and trilayers since, quite remarkably, Raman spectra can even be obtained from a single layer of carbon atoms (due to strong resonance Raman scattering in this material (Ferrari et al, 2006)). Moreover, graphene samples with different numbers of layers show significant differences in their Raman spectra as can be seen in Figure 4.4. In the case of single layer graphene, the G' (or 2D) Raman band is twice the intensity of the G band whereas in the two-layer material the G band is stronger than the 2D band. In addition, the 2D band is shifted to higher wavenumber in the two-layer graphene and has a different shape, consisting of 4 separate bands due to the resonance effects in the electronic structure of the 2-layer material (Ferrari et al, 2006). In fact it is possible to use Raman spectroscopy to determine the stacking order in several layers of graphene (for instance to distinguish between two separate single layers overlapping and a graphene bilayer in which the original Bernal crystallographic stacking is retained (Young et al, 2012)). As the number of layers is increased the 2D band moves to higher wavenumber and becomes broader and more asymmetric in shape for more than around 5 layers very similar to the 2D band of graphite. It should also be noted that in the Raman spectra shown in Figure 4.4 the D band, which is normally found in different forms of graphitic carbon due the presence of defects, is not present indicating that the mechanically-exfoliated graphene used to obtain the spectra in Figure 4.4 has a very high degree of perfection (Ferrari et al, 2006). More prominent D bands are found in samples of imperfect or damaged graphene such as some CVD material or in the vicinity of edges of small exfoliated fragments.

4.2.3. Mechanical properties

Lee et al (2009) undertook the direct determination of the mechanical properties of monolayer graphene through the nanoindentation of graphene membranes, suspended over holes of 1.0 - 1.5 μm in diameter on a silicon substrate, in an atomic force microscope (AFM). They isolated the monolayers through the use of optical microscopy and identified them with Raman spectroscopy. They determined the variation of force with indentation depth and derived stress-strain curves by assuming that the graphene behaved mechanically as a 2D membrane of thickness 0.335 nm. It was found that failure of the graphene took place by the bursting of the single molecular layer membrane at large displacements with failure initiating at the indentation point. The stress-strain curve for the graphene derived from the analysis of the indentation experiments is shown in Figure 4.5. It can be seen that the stress-strain curve becomes non-linear with increasing strain and that fracture occurs at a strain of well over 20%.

Using density functional theory, Liu, Ming and Li (2007) had earlier undertaken an ab initio calculation of the stress-strain curve of a graphene single layer. This is

also plotted in Figure 4.5 and it can be seen that there is extremely good agreement between the theoretical analysis and the experimentally-derived curve. The value of Young's modulus determined from the indentation experiment (Lee et al, 2009) is 1000 ± 100 GPa and this compares very well with the theoretical estimate (Liu, Ming and Li, 2007) of 1050 GPa. It is also similar to the value of 1020 GPa determined many years ago for the Young's modulus of bulk graphite In addition, the strength of the graphene monolayer was determined experimentally to be up to 130 ± 10 GPa. This is the order of $E/8$, where E is the Young's modulus, and so is close to the theoretically-predicted value of the strength of a defect-free material (Kelly and Macmillan, 1986).

The theoretical failure stress can also be determined from the maximum stress in the calculated stress-strain curve in Figure 4.5. Liu, Ming and Li (2007) found that the behaviour of the graphene at high-strains should differ slightly depending upon the crystallographic direction in which the graphene is deformed. They predicted the strength to be in the range 107 - 121 GPa, which is again in very good agreement with the range of values measured experimentally.

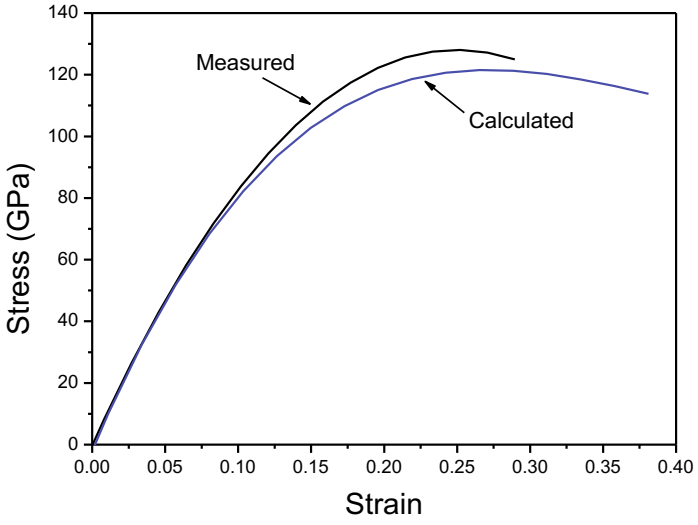

Figure 4.5. Measured (Lee et al, 2009) and calculated (Liu, Ming and Li, 2007) stress-strain curve for the deformation of a graphene monolayer.

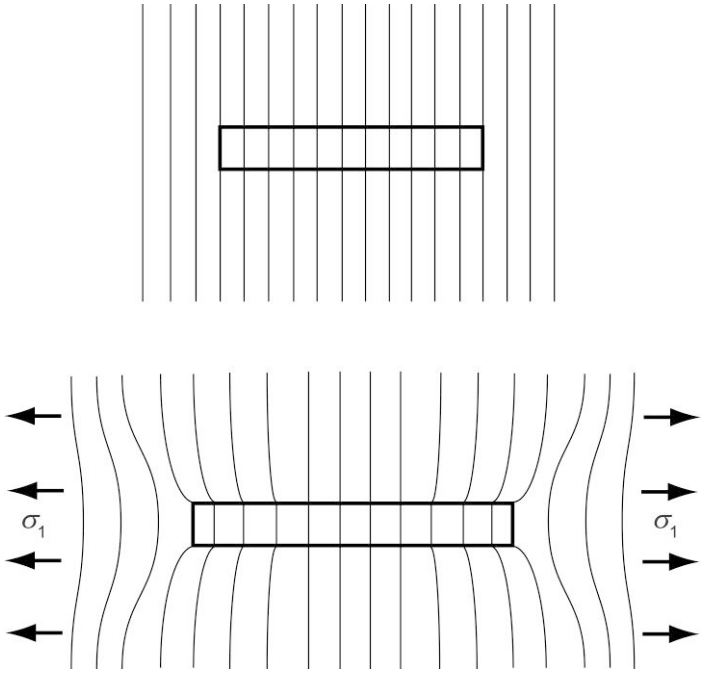

Figure 4.6. Deformation patterns for a discontinuous graphene flake in a low-modulus polymer matrix. The top diagram shows the situation before deformation and the bottom diagram shows the effect of the application of a tensile stress, σ_1, parallel to the flake. (Adapted from Gong et al., 2010 with permission from Wiley-VCH).

4.3. Nanoplatelet Reinforcement – Theory

In view of the growing interest in the study of polymer-based nanocomposites, it will be shown how the shear-lag methodology can be modified to predict the distribution of stress and strain in nanoplatelets reinforcing a polymer matrix and an analogous set of relationships is obtained for nanoplatelet reinforcement to those obtained for fibre reinforcement. Because of the very strong resonance Raman scattering, it will be shown that well-defined Raman spectra can be obtained from graphene monolayers. Large stress-induced band shifts can be obtained from these sheets when embedded in a polymer matrix which has enabled the prediction of the shear lag model to be validated. It will be shown further how the shear-lag model (Cox, 1952; Kelly, 1966; Kelly and Macmillan, 1986) can be used to model reinforcement by few-layer graphene.

4.3.1. Micromechanics

It is of interest to see if the reinforcement of composites with nanoplatelets can also be analyzed using continuum mechanics. In the case of nanoplatelets such as a discontinuous graphene flake reinforcing a composite matrix, stress transfer from the matrix to the flake will also be assumed to take place through a shear stress at the flake/matrix interface (Gong et al., 2010). This can also be represented diagrammatically by Figure 4.6 where the rectangle in this case represents the two-dimensional section through a nanoplatelet in a matrix rather than along the middle of a fibre. Before deformation parallel lines perpendicular to the flake can again be drawn from the matrix through the flake before deformation. When the system is subjected to axial stress, σ_l, parallel to the flake axis, the lines become distorted since the Young's modulus of the matrix is much less than that of the flake. This induces a shear stress at the flake/matrix interface. The axial stress in the flake will build up from zero at the flake ends to a maximum value in the middle of the flake. The uniform strain assumption means that, if the flake is long enough, in the middle of the flake the strain in the flake equals that in the matrix. Since the nanoplatelets have a much higher Young's modulus it means that the nanoplatelets carry most of the stress, and therefore load, in the composite.

The relationship between the interfacial shear stress, τ_i, near the flake ends and the flake stress, σ_f, can be determined by using a force balance of the shear forces at the interface and the tensile forces in a flake element as shown in Figure 4.7. The main assumption is that the forces due to the shear stress at the interface, τ_i, is balanced by the force due to the variation of axial stress in the flake, $d\sigma_f$, such that if the element shown in Figure 4.7 is of unit width

$$\tau_i dx = t d\sigma_f \tag{4.1}$$

and so

$$\frac{d\sigma_f}{dx} = \frac{\tau_i}{t} \tag{4.2}$$

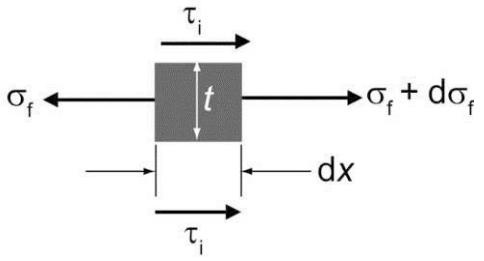

Figure 4.7. Balance of stresses acting on an element of length, d*x*, of the flake of thickness, *t*, in the composite. (Adapted from Gong et al., 2010 with permission from Wiley-VCH).

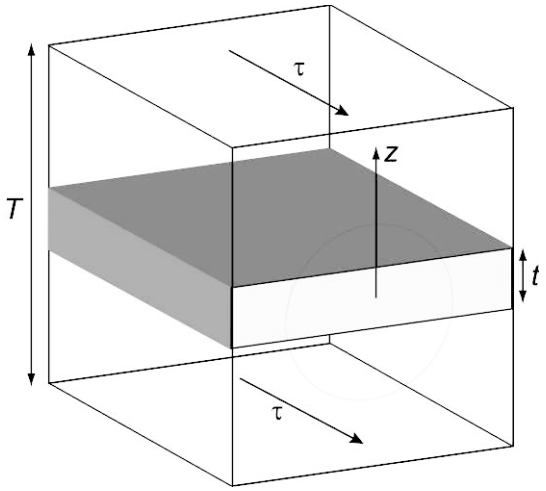

Figure 4.8. Model of a flake within a resin used in shear-lag theory. The shear stress τ acts at a distance z from the flake centre. (Adapted from Gong et al., 2010 with permission from Wiley-VCH).

The behaviour of a discontinuous flake in a matrix can be modelled using shear lag theory in which it is assumed that the flake is surrounded by a layer of resin at a distance, z, from the flake centre as shown in Figure 4.8. The resin has an overall thickness of T. It is assumed that both the flake and matrix deform elastically and the flake-matrix interface remains intact. If u is the displacement of the matrix in the flake axial direction at a distance, z, then the shear strain, γ, at that position is be given by

$$\gamma = \frac{\mathrm{d}u}{\mathrm{d}z} \tag{4.3}$$

The shear force per unit length carried by the matrix is transmitted to the flake surface though the layers of resin and so the shear strain at any distance z is given by

$$\frac{\mathrm{d}u}{\mathrm{d}z} = \frac{\tau_\mathrm{i}}{G_\mathrm{m}} \tag{4.4}$$

This equation can be integrated using the limits of the displacement at the flake surface ($z = t/2$) of $u = u_\mathrm{f}$ and the displacement at $z = T/2$ of $u = u_\mathrm{T}$

$$\int_{u_f}^{u_T} \mathrm{d}u = \frac{\tau_\mathrm{i}}{G_\mathrm{m}} \int_{t/2}^{T/2} \mathrm{d}z \tag{4.5}$$

hence $$u_\mathrm{T} - u_\mathrm{f} = \left(\frac{\tau_\mathrm{i}}{2G_\mathrm{m}}\right)(T - t) \tag{4.6}$$

It is possible to convert these displacements into strain since the flake strain, e_f and matrix strain, e_m, can be approximated as $e_\mathrm{f} \approx \mathrm{d}u_\mathrm{f}/\mathrm{d}x$ and $e_\mathrm{m} \approx \mathrm{d}u_\mathrm{T}/\mathrm{d}x$. It should be noted again that this shear-lag analysis is not rigorous but it serves as a simple illustration of the process of stress transfer from the matrix to a flake in a graphene-flake composite. In addition, τ_i is given by Equation (4.2) and so differentiating Equation (4.6) with respect to x leads to

$$e_\mathrm{f} - e_\mathrm{m} = \frac{tT}{2G_\mathrm{m}} \frac{\mathrm{d}^2\sigma_\mathrm{f}}{\mathrm{d}x^2} \tag{4.7}$$

since $T >> t$. Multiplying through by E_f gives

$$\frac{\mathrm{d}^2\sigma_\mathrm{f}}{\mathrm{d}x^2} = \frac{n^2}{t^2}\left(\sigma_\mathrm{f} - e_\mathrm{m}E_\mathrm{f}\right) \tag{4.8}$$

where $$n = \sqrt{\frac{2G_\mathrm{m}}{E_\mathrm{f}} \frac{t}{T}}$$

This differential equation has the general solution

$$\sigma_\mathrm{f} = E_\mathrm{f}e_\mathrm{m} + C\sinh\left(\frac{nx}{t}\right) + D\cosh\left(\frac{nx}{t}\right)$$

where C and D are constants of integration. This equation can be simplified and solved if it is assumed that the boundary conditions are that there is no stress transmitted across the flake ends, i.e. if $x = 0$ in the middle of the flake where $\sigma_\mathrm{f} = E_\mathrm{f}e_\mathrm{m}$ then $\sigma_\mathrm{f} = 0$ at $x = \pm l/2$. This leads to $C = 0$ and

$$D = \frac{E_\mathrm{f}e_\mathrm{m}}{\cosh(nl/2t)}$$

The final equation for the distribution of flake stress as a function of distance, x along the flake is then

$$\sigma_\mathrm{f} = E_\mathrm{f}e_\mathrm{m}\left(1 - \frac{\cosh(nx/t)}{\cosh(nl/2t)}\right) \tag{4.9}$$

4.3.2. Interfacial Shear Stress

Finally it is possible to determine the distribution of interfacial shear stress along the flake using Equation (4.2) which leads to

$$\tau_i = nE_f e_m \frac{\sinh(nx/t)}{\cosh(nl/2t)} \tag{4.10}$$

It is convenient at this stage to reintroduce the concept of flake aspect ratio, defined in this case as $s = l/t$ so that the two equations above can be rewritten as

$$\sigma_f = E_f e_m \left[1 - \frac{\cosh\left(ns\frac{x}{l}\right)}{\cosh(ns/2)}\right] \tag{4.11}$$

for the axial flake stress and as

$$\tau_i = nE_f e_m \left[\frac{\sinh\left(ns\frac{x}{l}\right)}{\cosh(ns/2)}\right] \tag{4.12}$$

for the interfacial shear stress.

It can be seen that the nanoplatelet is most highly stressed, i.e. the most efficient flake reinforcement is obtained, when the product ns is high. This implies that a high aspect ratio, s, is desirable along with a high value of n. The similarity of this analysis for the nanoplatelet to the shear lag analysis for a fibre and of the equations derived is remarkable. The reason for this is that the shear-lag analysis considers only axial stresses and the shear-lag model represented by Figure 4.6 is applicable to both situations.

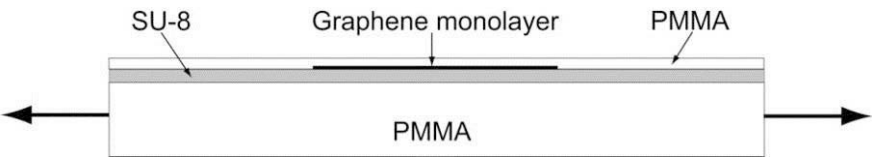

Figure 4.9 Schematic diagram (not to scale) of a section through a single monolayer graphene composite. (Adapted from Gong et al., 2010 with permission from Wiley-VCH).

4.4. Nanoplatelet Reinforcement – Experiment

As in the case of carbon fibres (Montes-Morán and Young, 2002), Raman spectroscopy can be employed to follow the micromechanics of reinforcement by graphene nanoplatelets in nanocomposites (Gong et al, 2010). Figure 4.9 shows a schematic diagram of a model composite specimen consisting of a single graphene monolayer sandwiched between two polymer layers. The SU-8 epoxy was spin-coated onto a poly(methyl methacrylate) (PMMA) beam and allowed to cure. The graphene monolayer was produced by repeated cleavage of a graphite crystal with adhesive tape and pressed onto the beam. The PMMA top coat was spin coated to seal the monolayer on the beam. Deformation was applied by bending the PMMA beam and monitoring the matrix strain using a resistance strain gauge (Gong et al, 2010).

4.4.1. Monolayer graphene

Graphene undergoes very strong resonance Raman scattering (Malard et al, 2009) which means that it is possible to obtain a spectrum from a single-atom thick monolayer embedded in several microns of PMMA (Gong et al, 2010). Figure 4.4 shows a Raman spectrum obtained from a single graphene monolayer. It can be seem that it consists of two sharp bands with the 2D band being characteristically stronger than the G band for the monolayer (Ferrari et al, 2006). The absence of a D band also shows that the graphene is relatively free of defects.

The 2D band is found to shift to lower wavenumber with tensile deformation as shown in Figure 4.10. It can be seen that there is a large, approximately linear shift of the band, with a shift rate of the order of -60 cm^{-1}/% strain. Cooper et al (2001) found that there was a simple linear relationship between the 2D band position for carbon fibres. Assuming that the relationship for carbon fibres between band shift rate and Young's modulus determined by Cooper et al (2001) is also applicable to monolayer graphene, this would imply that the graphene has a Young's modulus in excess of 1000 GPa, which is similar to the value determined by direct measurement (Lee et al, 2008).

As with carbon fibres (Montes-Morán and Young, 2002), the relationship shown in Figure 4.10(b) can also be used in a number of different situations to determine stress or strains distributions in graphene nanoplatelets in nanocomposites (Young et al, 2012). Examples of this approach will now be presented.

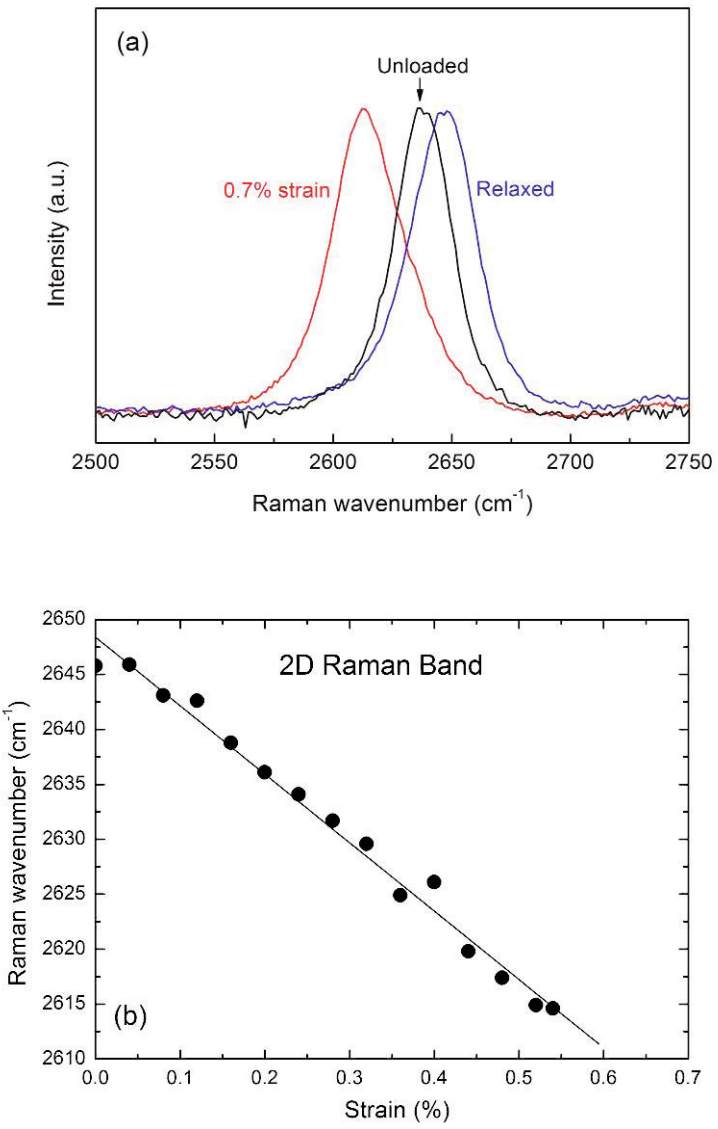

Figure 4.10. Effect of tensile deformation upon the position of the 2D Raman band for a graphene monolayer. (a) Shift of the band with a strain of 0.7%. (b) Shift of the band as a function of strain. (Adapted from Gong et al., 2010 with permission from Wiley-VCH).

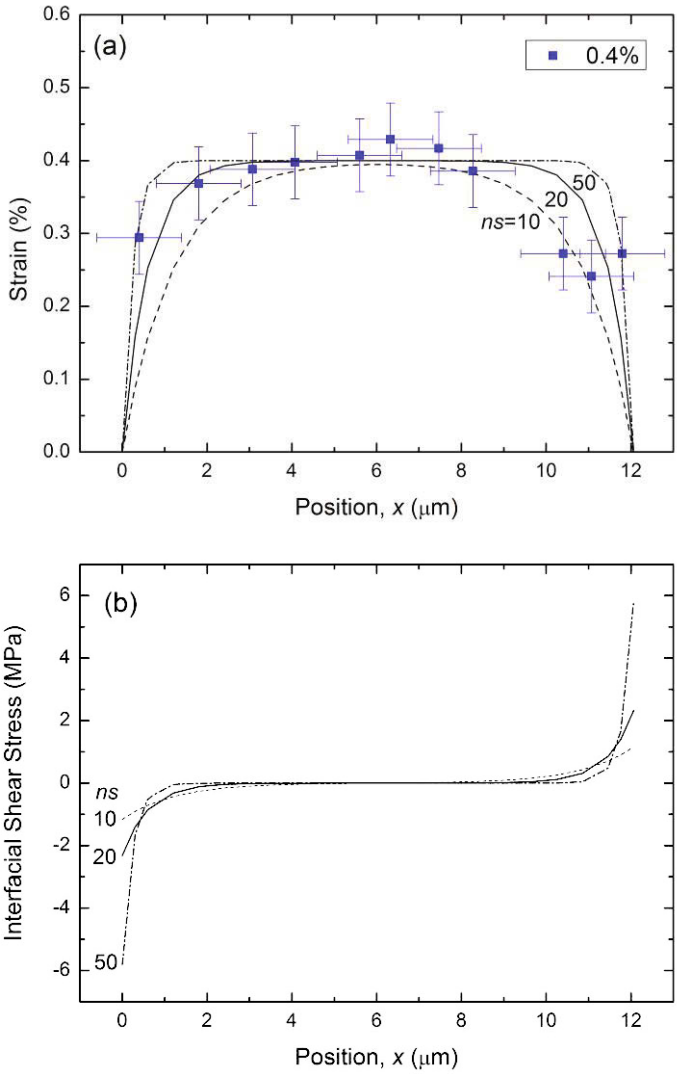

Figure 4.11. (a) Distribution of strain at 0.4% matrix strain in direction of the tensile axis across a graphene monolayer. The curves are fits of Equations (4.11) (b) Variation of interfacial shear stress with position determined from Equation (4.12). (Adapted from Gong et al., 2010 with permission from Wiley-VCH).

The experimental data on the variation of graphene strain across the middle of a monolayer flake are shown in Figure 4.11(a). The data were fitted to Equation (4.11) from the shear lag analysis derived above (Gong et al, 2010). It can be seen that the fits of the theoretical shear-lag curves to the strain distribution are sensitive to the value of *ns* chosen. The derived interfacial shear stress distributions are shown in Figure 4.11(b) and the value of interfacial shear stress at the flake ends is also very sensitive to the values of *ns* chosen. The best fit to the experimental data is for an *ns* value of 20, giving a maximum interfacial shear stress of around 2 MPa, well below the value of 50 MPa found for the carbon fibres (Montes-Morán and Young, 2002). The graphene has an inert atomically-smooth surface such that any interactions with the polymers will be through van der Waals bonding. The T50-O carbon fibres used by Montes-Morán and Young (2002) on the other had been plasma oxidized and had rough surfaces, leading to much stronger bonding with the polymer matrix. In the case of fibres that had not received the plasma oxidation treatment, lower levels of interfacial shear stress, approaching those found in similar investigations upon graphene, were obtained (Montes-Morán and Young, 2002).

Young et al (2011) showed in a further study, that the strain distribution in a single graphene atomic layer sandwiched between two thin layers of polymer on the surface of a PMMA beam (Figure 4.9) could be mapped in two dimensions with a high degree of precision from Raman band shifts as shown in Figure 4.12. The distribution of strain across the graphene monolayer was found to be relatively uniform at levels of matrix strain up to ~0.6% strain but that it became highly non-uniform above this strain. This change in strain distribution was shown (Young et al, 2011) to be due to a fragmentation process as a result of the development of cracks, most likely in the polymer coating layers, with the graphene appearing to remain intact. Between the cracks, the strain distributions in the graphene were approximately triangular in shape and the interfacial shear stress, τ_i, in the fragments was found to be only about 0.25 MPa. This is an order of magnitude lower than the interfacial shear stress before fragmentation (Gong et al, 2010). This relatively poor level of adhesion between the graphene and polymer layers again has important implications for the use of graphene in nanocomposites.

Although these investigations upon monolayer graphene have produced interesting an important insight into the reinforcement of polymers by graphene, large-scale graphene production invariably produces few-layer material. The behaviour of this material will be considered next.

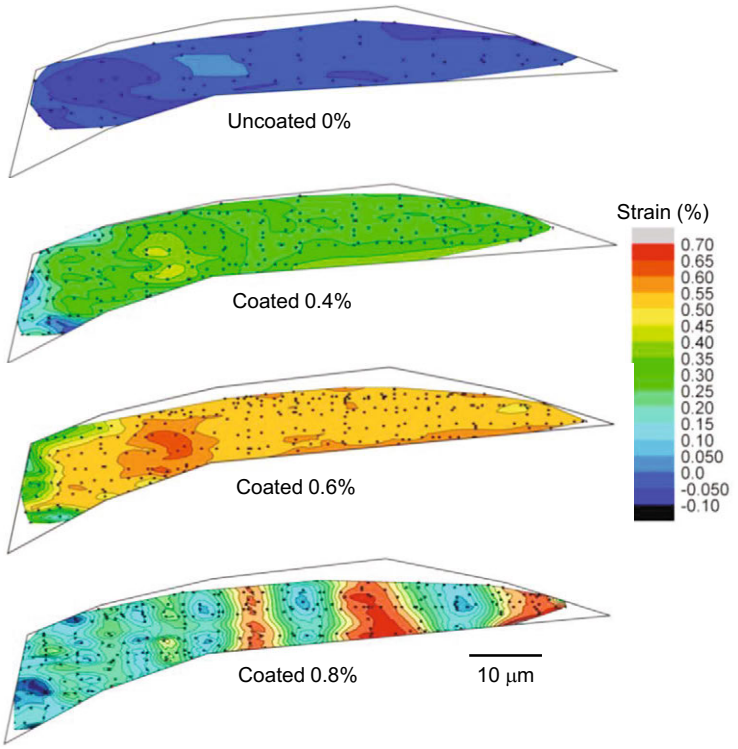

Figure 4.12. Contour maps of strain mapped over the graphene monolayer in a model composite. Maps are shown for the original flake before coating with the top polymer layer and then after coating with the top polymer layer at different levels of matrix strain indicated. (Adapted from Young et al, 2011 with permission from the American Chemical Society).

4.4.2. Few-layer Graphene

The deformation micromechanics of few-layer graphene in composites has also been investigated using Raman spectroscopy as shown in Figure 4.13 (Gong et al, 2012). The distribution of strain across a graphene flake containing both monolayer and bilayer regions is shown in Figure 4.13(a). This shows two important findings. Firstly the data can again be fitted well to the shear-lag model (Equation (4.11)). Secondly it can be seen that the strain in the bilayer regions is identical to that in adjacent monolayer regions. Figure 4.13(b) shows the strain distribution across a bilayer flake that has fragmented due probably to cracking in the polymer coating

(Gong et al, 2012). In this case triangular strain distributions are obtained, indicating damage to the interface and stress transfer by frictional sliding.

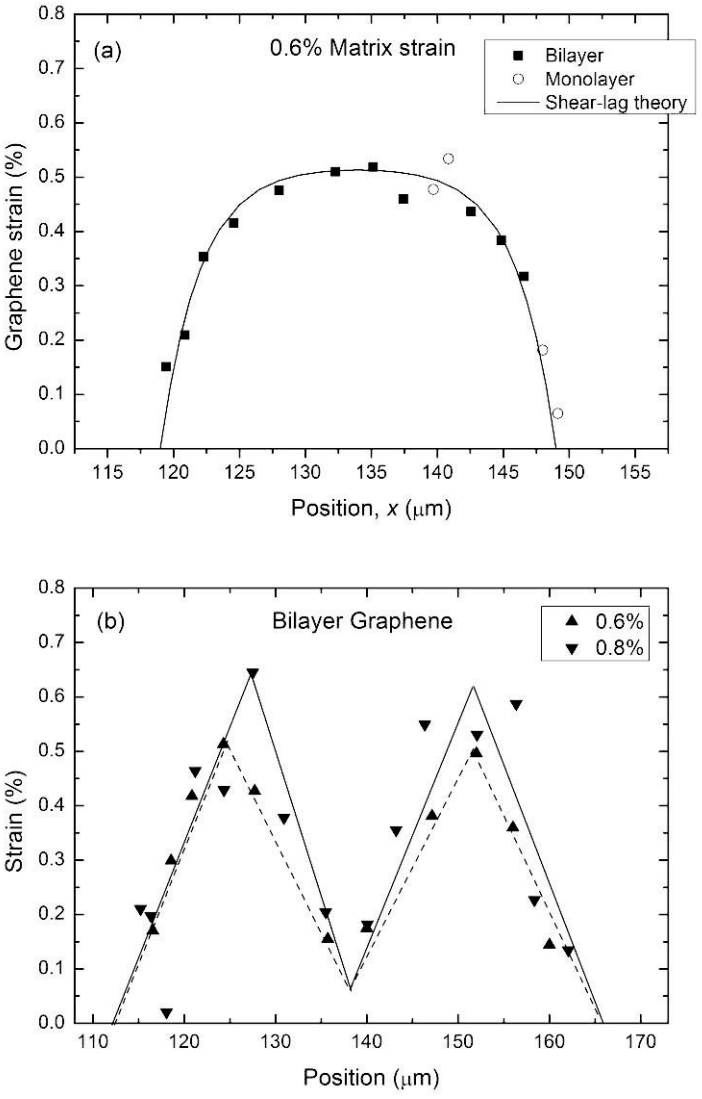

Figure 4.13. Distributions of strain at different matrix strain levels in the direction of the tensile axis across a graphene nanoplatelet. (a) Region with both monolayer and bilayer graphene at 0.6% matrix strain. (b) Bilayer region showing the effect fragmentation at 0.6% and 0.8% strains. (Adapted from Gong et al, 2012 with permission from the American Chemical Society).

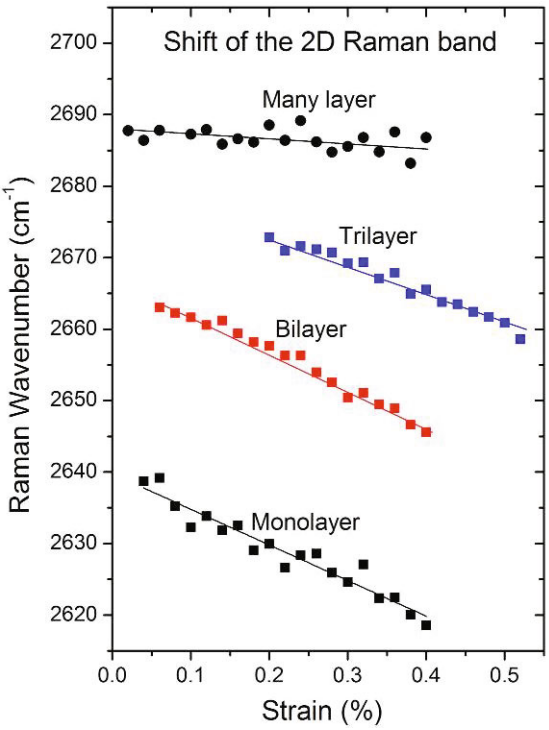

Figure 4.14. Shifts with strain of the 2D band for adjacent monolayer, bilayer and trilayer regions along with the shift with strain for the same band of a multilayer flake on the same specimen. (Adapted from Gong et al, 2012 with permission from the American Chemical Society).

Gong et al (2012) also undertook a systematic study of the deformation of bilayer, trilayer and many-layer graphene with a view to determining the optimum number of layers for the reinforcement of nanocomposites with graphene. The rate of 2D band shift per unit strain for uncoated bilayer graphene on a PMMA beam was found lower

to be than that for a monolayer, implying relatively poor stress transfer between the two layers in the bilayer material. In a subsequent paper Gong et al (2013) demonstrated clearly that the poor stress transfer between the layers in few-layer graphene is due to the reversible loss of Bernal stacking that takes place during shear deformation of the material.

The effect of coating the graphene was also investigated (Gong et al, 2012) and it was found that in this case the shift rate of the monolayer and bilayer material was the same. Measurements were also undertaken in the middle of adjacent monolayer, bilayer and trilayer regions of the same coated graphene flake up to 0.4% strain. The 2D band shifts with strain of these four different coated graphene structures are given in Figure 4.15. The slopes of the plots are similar for the monolayer and bilayer material but somewhat lower for the trilayer. In contrast, the slope for the many-layer graphene is significantly lower at only around -8 cm^{-1}/% strain. These findings were interpreted Gong et al (2012) as indicating that there was good stress transfer at the polymer-graphene interface but there were poorer levels of stress transfer between the graphene layers.

Gong et al (2012) adapted the theory of Zalamea et al (2007) for multi-walled nanotubes to quantify the stress transfer efficiency between the individual layers within graphene and considered first of all the advantages of using bilayer graphene rather than the monolayer material. In the case of two monolayer flakes dispersed well in a polymer matrix, the closest separation they can have will be controlled by the dimensions of the polymer coil, i.e. at least several nm (Gong et al, 2012). The separation between the two atomic layers in bilayer graphene is, however, only around 0.34 nm. It will therefore be easier to achieve higher loadings of bilayer material in a polymer nanocomposite which will lead to an improvement in reinforcement ability by up to a factor of two over monolayer material.

The optimum number of layers needed in many-layer graphene flakes for the best levels of reinforcement in polymer-based nanocomposites was also determined (Gong et al, 2012) The effective Young's modulus of monolayer and bilayer graphene will be similar and it will decrease as the number of layers decreases. For high volume fraction nanocomposites it will be necessary to accommodate the polymer coils between the graphene flakes. The separation of the flakes will be limited by the dimensions of the polymer coils as shown in Figure 4.15 and their minimum separation will depend upon the type of polymer and its interaction with the graphene. This is unlikely to be less than 1 nm and more likely several nm whereas the separation of the layers in multilayer graphene is only around 0.34 nm. In an ideal case, therefore, the nanocomposite can be assumed to be made up of parallel graphene flakes that are separated by thin layers of polymer, as shown in Figure 4.15.

The Young's modulus, E_c, of such as nanocomposite can be estimated to a first approximation using the simple "rule-of-mixtures" (Young and Lovell, 2011; Gibson, 2012) such that

$$E_c = E_{eff} V_g + E_m V_m \tag{4.13}$$

where E_{eff} is the effective Young's modulus of the multilayer graphene, E_m is the Young's modulus of the matrix (~3 GPa), and V_g and V_m are the volume fractions of the graphene and matrix polymer respectively. The maximum nanocomposite Yo ung's modulus can be determined using this equation for different numbers of graphene layers, as a function of the polymer layer thickness. The modulus is found to peak for three-layer graphene for a 1 nm polymer layer thickness and then decrease. The maximum nanocomposite Young's modulus is found to be virtually constant for composites with more than four graphene layers.

In summary, it was suggested by Gong et al (2012) that monolayer material does not necessarily give the best reinforcement and that the optimum number of graphene layers for the best reinforcement will depend upon the polymer layer thickness and the efficiency of stress transfer between the graphene layers.

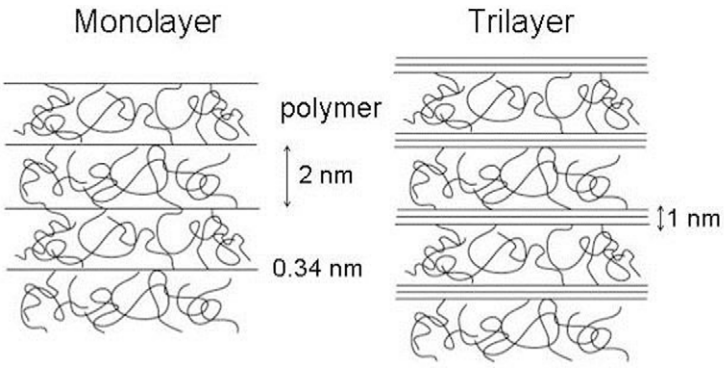

Fig. 8.15. Schematic diagram of the microstructure of graphene-based nanocomposites based upon either monolayer or trilayer reinforcements. The interlayer spacing of the graphene is 0.34 nm and the effective thickness of the polymer coils is assumed to be to be around 2 nm. (Adapted from Gong et al, 2012 with permission from the American Chemical Society).

4.5. Conclusions

A clear conclusion of this study is that the micromechanics of deformation of graphene nanoplatelets can be analyzed in terms of the shear-lag theory developed originally for fibre reinforcement. Although the analysis of fibre reinforcement has been taking place for over 50 years, it is still not yet fully understood. The study of

nanoplatelelet reinforcement in nanocomposites has been undertaken over a much a shorter period and so is far less well-developed. It has been shown that it appears that continuum mechanics is still applicable at the nanoscale and so much of the analysis undertaken for macroscopic composites can be employed and adapted. Nevertheless it remains to be seen how far it is possible, at the nanoscale, to use this analytical methodology and when it is necessary to employ numerical techniques such as the finite element method.

There are again a variety of different challenges that exist in developing micromechanics at the nanoscale that include:

- Axial compression. It is not clear how nanoplatelets respond to in-plane compression and what deformation modes lead to ultimate failure.
- Nanoplatelelet/nanoplatelelet interactions, including restacking. The effect of nanoplatelet separation and restacking upon mechanical properties is yet to be analysed.
- Nanoplatelelet /crack interactions. This is an area that has not yet been explored.
- Effect of nanoplatelelet orientation, waviness and wrinkling. It is thought that waviness and wrinkling may lead to inferior mechanical properties for nanoplatelelet-reinforced nanocomposites but this is yet to be put on a firm theoretical foundation.
- Effect of nanoplatelelet surface treatment and modification. It is highly likely that the chemical modification of nanoplatelelet surfaces will affect stress transfer in nanocomposites but no systematic studies have yet been undertaken.

Many of these problems and issues are similar at both the macroscopic and nanoscales. Some of them are different but the finding outlined in the present chapter that continuum mechanics is still applicable for the understanding of nanomechanics gives us confidence that there are good prospects that further rapid progress will be made in the years to come.

References

Avouris P. (2010). Graphene: Electronic and photonic properties and devices. *Nano Letters*, 10:4285-4294.

Bae S., Kim H. K., Lee Y. B., Xu X. F., Park J.-S., Zheng Y., Balakrishnan J., Lei T., Kim H. R., Song Y. I., Kim Y.-J., Kim K. S., Özyilmaz B., Ahn J.-H., Hong B. H., and Iijima S. (2010). Roll-to-roll production of 30-inch graphene films for transparent electrodes. *Nature Nanotechnology*, 5:574-578.

Bangert U., Gass M. H., Bleloch A. L., Nair R. R., and Geim A. K. (2009). Manifestation of ripples in free-standing graphene in lattice images obtained in an aberration-corrected scanning transmission electron microscope. *Physics Status Solidi A*, 206:1117–1122.

Booth T. J., Blake P., Nair R. R., Jiang D., Hill E. W., Bangert U., Bleloch A., Gass M., Novoselov K. S., Katsnelson M. I., and Geim A. K. (2008), Macroscopic graphene membranes and their extraordinary stiffness. *Nano Letters*, 8:2442-2446.

Cooper C. A., Young R. J., and Halsall M. (2001). Investigation into the deformation of carbon nanotubes and their composites through the use of Raman spectroscopy. *Composites A: Applied Science and Manufacturing*, 32:401-411.

Cox H. L. (1952). The elasticity and strength of paper and other fibrous materials. *British Journal of Applied Physics*, 3:72-79.

Ferrari A. C., Meyer J. C., Scardaci V., Casiraghi C., Lazzeri M., Mauri F., Piscanec S., Jiang D., Novoselov K. S., Roth S., and Geim A. K. (2006). Raman spectrum of graphene and graphene layers. *Physical Review Letters*, 97:187401.

Geim A. K., and Novoselov K. S. (2007). The rise of graphene. *Nature Materials*, 6:183-190.

Geim A. K. (2011). Nobel Lecture: Random walk to graphene. *Reviews of Modern Physics*, 83:851-862.

Gibson R. F. (2012). *Principles of Composite Material Mechanics*, 3rd Edition, CRC Press, Boca Raton.

Gong L., Kinloch I. A., Young R. J., Riaz I., Jalil R., and Novoselov K. S. (2010). Interfacial stress transfer in a graphene monolayer nanocomposite. *Advanced Materials*, 22:2694-2697.

Gong L., Young R. J., Kinloch I. A., Riaz I., Jalil R., and Novoselov K. S., Optimizing the reinforcement of polymer-based nanocomposites by graphene. *ACS Nano*, 2012, 6:2086-2095.

Gong L., Young R. J., Kinloch I. A., Haigh S. J., Warner J. H., Hinks J. A., Xu Z. W., Li L., Ding F., Riaz I., Jalil R., and Novoselov K. S. (2013). Reversible loss of Bernal stacking during the deformation of few-layer graphene in nanocomposites. *ACS Nano*, 7:7287-7294.

Hernandez Y., Nicolosi V., Lotya M., Blighe .F M., Sun Z. Y., De S., McGovern I. T., Holland B., Byrne M., Gun'ko Y. K., Boland J. J., Niraj P., Duesberg G., Krishnamurthy S., Goodhue R., Hutchison J., Scardaci V., Ferrari A. C., and Coleman J. N. (2008). High-yield production of graphene by liquid-phase exfoliation of graphite, *Nature Nanotechnology*, 3:563-568.

Kalaitzidou K., Fukushima H., Drzal L. T. (2007). A new compounding method for exfoliated graphite–polypropylene nanocomposites with enhanced flexural properties and lower percolation threshold. *Composites Science and Technology*, 67:2045–2051.

Kelly A. (1966). *Strong Solids*, Clarendon Press, Oxford.

Kelly A., and Macmillan N. H. (1986). *Strong Solids*, 3rd Edition, Clarendon Press, Oxford.

Lee C., Wei X. D., Kysar J. W., and Hone J. (2008). Measurement of the elastic properties and intrinsic strength of monolayer graphene. *Science*, 321:385-388.

Liu F., Ming P. B. and Li J. (2007). *Ab initio* calculation of ideal strength and phonon instability of graphene under tension. *Physical Review B*, 76:064120.

Malard L. M., Pimenta M. A., Dresselhaus G., and Dresselhaus M. S. (2009). *Physics Reports-Review Section of Physics Letters*. 473:51-87.

Meyer J. C., Geim A. K., Katsnelson M. I., Novoselov K. S., Booth T. J., and Roth S. (2007). The structure of suspended graphene sheets. *Nature*, 446:60-63.

Montes-Morán M. A., and Young R. J. (2002). Raman spectroscopy study of HM carbon fibres: effect of plasma treatment on the interfacial properties of single fibre/epoxy composites, Part II: Characterisation of the fibre/matrix interface. *Carbon*, 40:857-875.

Nair R. R., Blake P., Grigorenko A. N., Novoselov K. S., Booth T. J., Stauber T., Peres N. M. R., and Geim A. K. (2008). Fine structure constant defines visual transparency of graphene. *Science*, 320:1308.

Novoselov K. S., Geim A. K., Morozov S. V., Jiang D., Zhang Y., Dubonos S. V., Grigorieva I. V., and Firsov A. A. (2004). Electric field effect in atomically thin carbon films. *Science*, 306:666-669

Novoselov K. S. (2011). Nobel Lecture: Graphene: Materials in the flatland. *Reviews of Modern Physics*. 83:837-849.

Rao C. N. R., Biswas K., Subrahmanyam K. S., and Govindaraj A. (2009), Graphene, the new carbon. *Journal of Materials Chemistry*, 19:2457-2469.

Suk J. W., Kitt A., Magnuson C. W., Hao Y., Ahmed S., An J., Swan A. K., Goldberg B. B., and Ruoff R. S. (2011). Transfer of CVD-grown monolayer graphene onto arbitrary substrates. *ACS Nano*, 5:6916-6924

Young R. J. (1995). Monitoring deformation processes in high-performance fibres using Raman spectroscopy. *Journal of the Textile Institute*, 86:360-381.

Young R. J., Gong L., Kinloch I. A., Riaz I., Jalil R., and Novoselov K. S. (2011). Strain mapping in a graphene monolayer nanocomposite. *ACS Nano*, 5:3079-3084.

Young R. J., Kinloch I. A., Gong L., and Novoselov K. S. (2012). The mechanics of graphene nanocomposites: A review. *Composites Science and Technology*, 72:1459–1476.

Young R. J., and Lovell P. A. (2011). *Introduction to Polymers*, CRC Press, Boca Raton, Chapter 24.

Zalamea L., Kim H., and Pipes R. B. (2007). Stress transfer in multi-walled carbon nanotubes. *Composites Science and Technology*, 67:3425-3433.